

PART III
EXPERIMENTAL RESULTS

PART III – EXPERIMENTAL RESULTS

This part is divided in two sections. The first one (chapters 5 and 6) concerns the deposition and characterization of DLC films. These were grown by PECVD using a high-power pulsed-DC supply in a CH₄ atmosphere. The frequency range of operation is called medium-frequency (MF), and is comprised between 100 and 200 kHz. At higher frequencies, it is followed by high-frequency (HF), where RF (13.56 MHz) processes are involved. DC-pulsed discharges were studied by a Langmuir probe in time-resolved mode, so the plasma parameters have been tracked in every step of the power-pulse. The resulting DLC layers were deposited at a relatively high rate and showed slightly improved mechanical properties with respect to the RF-processed samples.

The second block describes the properties of DLC structures with metal contents, which were grown by two different deposition techniques. Alternating sputter magnetron deposition of metal and graphite targets led to Me/a-C multilayer structures (chapter 7), whereas reactive magnetron sputtering in an Ar-diluted CH₄ discharge provided metal-containing DLC films (chapter 8). The nanostructure of the samples has been systematically studied by TEM and has been related to other film properties. The aim is to obtain hard coatings and simultaneously resolve one of the main problems of DLC films: their bad adherence to substrates owing to the effect of high intrinsic stress.

Chapter 5

Plasma characterisation with a fast Langmuir probe

Chapter 5 -Plasma characterisation with a fast Langmuir probe

5.1. Introduction: methane glow discharge

Glow discharge modelling is motivated by the research in plasma processes at low pressure. The study of the complex phenomena that occur within plasmas leads the comprehension of deposition processes and, therefore, permits their optimization. Among the most popular hydrocarbon precursors destined to the deposition of DLC films by glow discharge decomposition, we can mention acetylene (C_2H_2) [Lin S.H., 1983], benzene (C_6H_6) [Joshi A., 1988], propane (C_3H_8) [Hallil A., 2000] and methane (CH_4), which is the most used [Lin S.H., 1983] [Lacerda R.G., 2002] [Andújar J.L., 2003]. Sputtering of a graphite target permits to synthesize hydrogen-free a-C, since no hydrogenated reactants are involved in this process.

It is a common task to mix the precursor with a rare gas to enhance ion bombardment onto substrate and, with this, modify the film properties. CH_4 plasmas highly diluted with Ar have been found to decrease the typically high concentration of $-CH_3$ radicals in CH_4 discharges to favour the presence of C_2H_n species [Riccardi C., 2001]. CH_4 has also been mixed with H_2 , and the resulting plasma has been characterised [Cherry R.I., 1995]. Investigations on CH_4/H_2 plasmas are of great interest in surface processing of microelectronic devices because of their intense etching action. In this introductory section, we will focus on pure methane plasma at low pressure for DLC coatings production.

Different approaches have been made in methane plasma modelling. The study of plasma chemistry has evolved in parallel with sophisticated simulation techniques and the accuracy of plasma diagnostics. Actually, weakly ionized plasma processes are characterized by a very large number of elementary reactions which involve a correspondingly large number of chemical species. Thus, a simplified model that highlights the basic phenomena in methane plasmas is required. Gogolides et al. developed a generalised model taking into account physical processes and chemistry of gas phase methane RF-plasma, which were combined in a self-consistent simulator [Gogolides E.,

1995]. On the other hand, Masi et al. [1998] built up a kinetic scheme which was described through a collection of species processed in several gas phase reactions, in which reversible thermal, electron impact, ionic and wall reactions are distinguished. The more recent model adopted by Herrebout et al. consists of simulating EEDF curves by solving 1-D balance equations for the densities of species in the plasma. The network of the gas phase most representative chemical reactions is summarized in table 5.1, in which neutral-neutral, ion-neutral and electron-neutral reactions are distinguished, together with their corresponding reaction rate coefficients, k [Herrebout D., 2001].

Electron-neutral reactions	k (10^{-16} m³/s)	Ion-neutral reactions	k (10^{-16} m³/s)
$\text{CH}_4 + e \rightarrow \text{CH}_4^* + e$	-	$\text{CH}_4^+ + \text{CH}_4 \rightarrow \text{CH}_5^+ + \text{CH}_3$	15.0
$\text{CH}_4 + e \rightarrow \text{CH}_4^+ + 2e$	340	$\text{CH}_3^+ + \text{CH}_4 \rightarrow \text{C}_2\text{H}_5^+ + \text{H}_2$	12.0
$\text{CH}_4 + e \rightarrow \text{CH}_3^+ + \text{H} + 2e$	320	$\text{CH}_5^+ + \text{C}_2\text{H}_6 \rightarrow \text{C}_2\text{H}_5^+ + \text{CH}_4 + \text{H}_2$	5.0
$\text{CH}_4 + e \rightarrow \text{CH}_3 + \text{H} + e$	450	$\text{H}_2 + \text{H}_2^+ \rightarrow \text{H}_3^+ + \text{H}$	25.0
$\text{CH}_4 + e \rightarrow \text{CH}_2 + 2\text{H} + e$	73	$\text{H}_3^+ + \text{CH}_4 \rightarrow \text{CH}_5^+ + \text{H}_2$	16.0
		$\text{H}_3^+ + \text{C}_2\text{H}_6 \rightarrow \text{C}_2\text{H}_5^+ + 2\text{H}_2$	20.0
$\text{H}_2 + e \rightarrow \text{H}_2^* + e$	-	$\text{H}_3^+ + \text{C}_2\text{H}_4 \rightarrow \text{C}_2\text{H}_5^+ + \text{H}_2$	19.0
$\text{H}_2 + e \rightarrow 2\text{H} + e$	-		
$\text{H}_2 + e \rightarrow \text{H}_2^+ + 2e$	-		
		Neutral-neutral reactions	
$\text{C}_2\text{H}_6 + e \rightarrow \text{C}_2\text{H}_6^* + e$	-	$\text{CH}_3 + \text{CH}_3 \rightarrow \text{C}_2\text{H}_6$	0.37
$\text{C}_2\text{H}_6 + e \rightarrow \text{C}_2\text{H}_4^+ + \text{H}_2 + 2e$	-	$\text{CH}_3 + \text{H} \rightarrow \text{CH}_4$	0.07
$\text{C}_2\text{H}_6 + e \rightarrow \text{C}_2\text{H}_5 + \text{H} + e$	-	$\text{C}_2\text{H}_5 + \text{H} \rightarrow \text{CH}_3 + \text{CH}_3$	0.6
		$\text{C}_2\text{H}_5 + \text{CH}_3 \rightarrow \text{C}_3\text{H}_8$	0.04
$\text{C}_3\text{H}_8 + e \rightarrow \text{C}_3\text{H}_8^* + e$	-	$\text{CH}_2 + \text{H} \rightarrow \text{CH} + \text{H}_2$	2.7
$\text{C}_3\text{H}_8 + e \rightarrow \text{C}_2\text{H}_4 + \text{CH}_4 + e$	-	$\text{CH} + \text{CH}_4 \rightarrow \text{C}_2\text{H}_5$	1.0
		$\text{CH}_2 + \text{CH}_4 \rightarrow \text{CH}_3 + \text{CH}_3$	0.17
$\text{C}_2\text{H}_4 + e \rightarrow \text{C}_2\text{H}_4^* + e$	-	$\text{CH}_2 + \text{CH}_4 \rightarrow \text{C}_2\text{H}_4 + \text{H}_2$	0.17
$\text{C}_2\text{H}_4 + e \rightarrow \text{C}_2\text{H}_4^+ + 2e$	-	$\text{CH}_4 + \text{CH} \rightarrow \text{C}_2\text{H}_4 + \text{H}$	1.0
$\text{C}_2\text{H}_4 + e \rightarrow \text{C}_2\text{H}_2 + 2\text{H} + e$	-	$\text{CH}_3 + \text{CH}_2 \rightarrow \text{C}_2\text{H}_4 + \text{H}$	0.33
		$\text{C}_2\text{H}_5 + \text{H} \rightarrow \text{C}_2\text{H}_4 + \text{H}_2$	0.03
$\text{C}_2\text{H}_2 + e \rightarrow \text{C}_2\text{H}_2^* + e$	-	$\text{CH}_2 + \text{CH}_2 \rightarrow \text{C}_2\text{H}_2 + \text{H}_2$	0.11
$\text{C}_2\text{H}_2 + e \rightarrow \text{C}_2\text{H}_2^+ + 2e$	-		

Table 5.1: Chemical processes in a CH₄ RF-glow discharge varying from 20 to 65 Pa [Herrebout D., 2001].

As shows table 5.1, the neutral species background in methane glow discharge conditions consists of CH₄, H₂, C₂H₆, C₃H₈, C₂H₄ and C₂H₂, being the four latter more abundant at high pressures. The considered ions are CH₄⁺, CH₃⁺, H₂⁺, CH₅⁺, C₂H₅⁺, H₃⁺, C₂H₄⁺, C₂H₂⁺, whereas C₂H₅, CH₃, CH₂, CH, and H form the radicals collection. According to simulation results taking into account the rate coefficients for reactions (Table 5.1), the most likely present hydrocarbon ions in methane plasma are CH₅⁺ and C₂H₅⁺. C₂H₅⁺ is the predominant ion at pressures higher than 25 Pa [Herrebout D., 2001]. Nevertheless, more

recent studies [Alexandrov A.L., 2005] show that CH_5^+ dominates in the deposition range of this thesis (~ 10 Pa). Since density of positive ions is about one order of magnitude higher than the negative ions, CH_4 plasma has a strong electropositive character. Methyl radicals and atomic hydrogen are the plasma species present in the largest amount. Concretely, the concentration of H atoms is enlarged by increasing the supplied power, owing to higher methane dissociation [Masi M., 1998].

The primary electron impact processes are the first five reactions in table 5.1. They directly involve CH_4 molecules and lead to excited states of this molecule, which in turn are dissociated and provide the most important source of radicals in the discharge. Such radicals are then available for the secondary ion-neutral and neutral-neutral reactions. Among the secondary processes, the ionisation reactions are responsible only for sustaining the plasma.

The growth process of DLC films from CH_4 plasmas has been simulated in the literature with a surface deposition model, which managed at both gas phase and surface levels elementary reactions concerning only CH_3 , CH_2 , H, CH_4 and H_2 radicals [Mantzaris N.V., 1996]. As shown in table 5.2, deposition is described by many surface processes: adsorption-desorption, direct incorporation of ionised methyl groups, hydrogen reemission, ion stitching, adsorbed layer reactions, surface etching and sputtering. Ion stitching is the process in which adsorbed neutral radicals are chemically bonded with the film by collisions with ions from the plasma. Coefficients c_b and y_{ch} refer to the physical variables H/C ratio and yield of H sputtering, respectively. Ion stitching process is found to dominate the deposition rate for intermediary energy values (100-850 eV), while direct ion incorporation is predominant above 850 eV, in competition with increasing sputtering. More details about DLC growth are given in chapter 2.

Adsorption	Ion-induced incorporation of neutrals (stitching)
$\text{CH}_3(\text{plasma}) \rightarrow \text{CH}_3(\text{ads})$	$\text{CH}_4^+ + \text{CH}_3(\text{ads}) \rightarrow \text{C}_{(\text{s})} + \text{H}_{(\text{s})} + \text{H}_2(\text{plasma}) + \text{CH}_4^+$
$\text{CH}_2(\text{plasma}) \rightarrow \text{CH}_2(\text{ads})$	$\text{CH}_3^+ + \text{CH}_3(\text{ads}) \rightarrow \text{C}_{(\text{s})} + \text{H}_{(\text{s})} + \text{H}_2(\text{plasma}) + \text{CH}_3^+$
$\text{H}_{(\text{plasma})} \rightarrow \text{H}_{(\text{ads})}$	$\text{CH}_4^+ + \text{CH}_2(\text{ads}) \rightarrow \text{C}_{(\text{s})} + \text{H}_2(\text{plasma}) + \text{CH}_4^+$
	$\text{CH}_3^+ + \text{CH}_2(\text{ads}) \rightarrow \text{C}_{(\text{s})} + \text{H}_2(\text{plasma}) + \text{CH}_3^+$
Desorption	
$\text{CH}_3(\text{ads}) \rightarrow \text{CH}_3(\text{des})$	Adsorbed layer reactions
$\text{CH}_2(\text{ads}) \rightarrow \text{CH}_2(\text{des})$	$\text{CH}_3(\text{ads}) + \text{H}_{(\text{plasma})} \rightarrow \text{CH}_4(\text{plasma})$
$\text{H}_{(\text{ads})} \rightarrow \text{H}_{(\text{des})}$	$\text{CH}_2(\text{ads}) + \text{H}_{(\text{plasma})} \rightarrow \text{CH}_3(\text{plasma})$
	$\text{H}_{(\text{ads})} + \text{H}_{(\text{plasma})} \rightarrow \text{H}_2(\text{plasma})$
Direct incorporation of CH_4^+ and CH_3^+	
$\text{CH}_4^+ \rightarrow \text{C}_{(\text{s})} + 2\text{H}_{(\text{s})} + \text{H}_2(\text{plasma})$	Surface etching reaction
$\text{CH}_3^+ \rightarrow \text{C}_{(\text{s})} + \text{H}_{(\text{s})} + \text{H}_2(\text{plasma})$	$\text{C}_{(\text{s})} + c_b\text{H}_{(\text{s})} + (4-c_b)\text{H}_{(\text{plasma})} \rightarrow \text{CH}_4(\text{plasma})$
Reemission of $\text{H}_{(\text{s})}$	Sputtering
$c_b\text{H}_{(\text{s})} \rightarrow 0.5y_{\text{ch}}\text{H}_2(\text{plasma}) + (c_b-y_{\text{ch}})\text{H}_{(\text{s})}$	$\text{C}_{(\text{s})} \rightarrow y_{\text{sp}}\text{C}_{(\text{plasma})} + (1-y_{\text{sp}})\text{C}_{(\text{s})}$

Table 5.2: Surface processes for the CH_4 discharge [Mantzaris N.V., 1996]

5.2. Study of a RF methane glow discharge

As introduced in chapter 2, the analysis of the growth stage of thin film materials provides data that can be related to their physical and chemical properties. Thus, we have analysed the deposition conditions of DLC films in the PECVD reactor. The environment of film deposition consisted of 10 Pa methane gas in glow discharge regime, whose parameters have been studied by a fast electrostatic probe described elsewhere (chapter 3).

5.2.1. I(V) characteristics

The DLC films were deposited onto c-Si substrates placed on the cathode. Since RF power was directly driven to the substrate holder (cathode), the bombardment conditions of film surface were controlled by the self-bias voltage acquired owing to electric signal. In this study, we adjusted bias voltage to -200, -400 and -600 V through the control system and acquired electric parameters of methane plasma by means of plasma diagnostics with Langmuir probe. These parameters were calculated by fitting the recorded $I(V)$ curves to the following model [Liebermann M.A., 2005]:

$$i_e = C\sqrt{V_p - V} + i_p \exp\left[\frac{e(V - V_p)}{kT_e}\right], \quad V < V_p \quad (5.1)$$

Here, i_e is the probe electron current; V is the probe bias; V_p is the plasma potential, identified as the potential of the maximum of the derivative of the experimental $I(V)$ curve; C is a constant; e is the elementary charge; k is the Boltzmann's constant; T_e is the electron temperature, and i_p is the electron current at plasma potential, which is related to the electron density, n_e :

$$i_p = n_e e A \left(\frac{kT_e}{2\pi m}\right)^{1/2} \quad (5.2)$$

where A is the area of the cylindrical probe (0.87 mm^2), and m is the electron mass ($9.109 \cdot 10^{-31} \text{ kg}$). However, it is not only electrons that contribute to the probe current, but there is an ionic component that also contributes. The first term in equation 5.1 gives account of the ion current saturation regime, and is equal to zero at probe bias voltages higher than the plasma potential. The constant C approaches to the magnetron conditions:

$$C = \frac{n_i A}{\pi} \sqrt{\frac{2e^3}{M}} \quad (5.3)$$

From this approximation, we estimate the ion density, n_i . On the other hand, the CH_5^+ ion is one of the most abundant in methane discharge, as mentioned in section 5.1. Hence, for all the calculations we have approached ion mass, M , to 17 a.m.u. ($17 \times 1.6726 \cdot 10^{-27}$ kg).

The optimization variables are n_i , n_e and T_e , namely the plasma parameters. Plasma potentials, V_p , have been determined from the maximum of the derivative experimental curve of $I(V)$ characteristics. Figure 5.1(a) plots the recorded $I(V)$ curves and figure 5.1(b) presents their corresponding derivatives below.

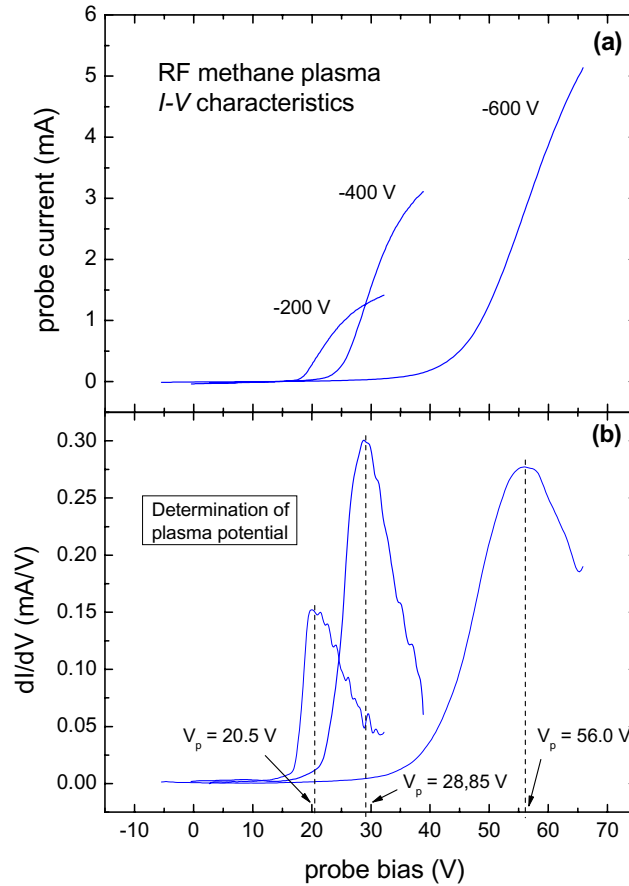


Figure 5.1: Determination of the plasma potentials corresponding to RF CH_4 glow discharges at different self-bias voltages.

Figure 5.2(a) shows the $I(V)$ characteristic corresponding to the RF methane plasma at -400 V bias along with the fitted curve. In figure 5.2(b), probe current is plotted in logarithmic scale to accurately fit the ionic saturation region. From these plots, we can check that the proposed model fits only for the probe bias region up to the plasma

potential. Above this value, our model diverges from the experimental data. This behaviour is evident from equation 5.1, which does not consider the electron current saturation regime of glow discharges at high positive probe bias. The current is limited by the generation of electrons inside the discharge and the dimensions of the probe tip. The electron density is controlled by the density of neutrals and the number of ionizing collisions. For our purposes, it is necessary to study the $I(V)$ characteristics below V_p .

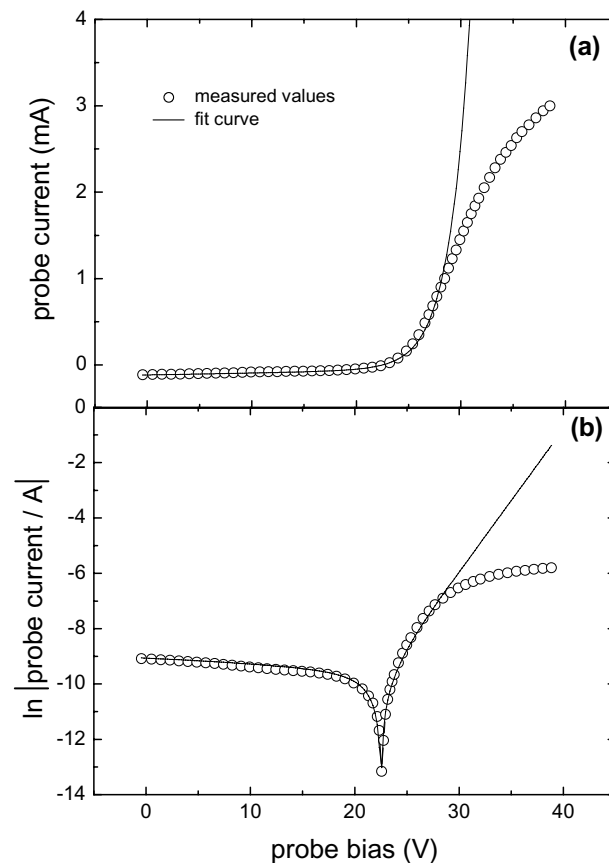


Figure 5.2: Measured probe characteristic from a RF CH_4 discharge and its fitted curve, plotted on (a) linear and (b) logarithmic scales.

5.2.2. Plasma parameters

The calculation of plasma parameters has been performed at three cathode self-bias voltages: -200, -400 and -600 V. Table 5.3 presents the evolution of plasma variables from the fittings. Electron temperature increases, along with self-bias, from 1.03 up to 5.34 eV in an exponential mode. Similarly, plasma potential varies from 20.5 to 56.5 V. Such increase in both parameters indicates a stronger ionisation of the methane discharge at higher cathode voltages. On the other hand, the great variation of required power to bias

the discharge from -400 to -600 V may explain the strong raisings of V_p and T_e . Electron and ion densities show interesting behaviours, attending to plasma quasi-neutrality. Their evolution is opposed: as expected, electron density is enhanced at higher self-bias, whereas progressive ion depletion occurs. Both curves coincide at approximately -600 V. Hence, plasma quasi-neutrality conditions are achieved at high supplied power.

Self-bias (V)	Supplied power (W)	Electron temperature (eV)	Electron density (10^9 cm^{-3})	Ion density (10^9 cm^{-3})	Plasma potential (V)	Floating potential (V)
-200	13	1.03	1.54	18.7	20.5	18.3
-400	43	1.94	4.68	15.3	28.85	22.5
-600	100	5.34	6.05	6.86	56.0	33.5

Table 5.3: Evolution of plasma parameters as a function of self-bias voltage and supplied power in a RF methane discharge.

We must pay special attention to the values acquired by Debye length. This parameter is defined in appendix C (equation C.24) and gives account of the distance at which electric field is screened by the spatial charge distribution. This expression is easier to handle if constants are substituted:

$$\lambda_{De} [cm] = 6.9 \cdot \sqrt{\frac{T_e [K]}{n_e [cm^{-3}]}} \quad (5.4)$$

The condition $\lambda_{De} \leq r_s$, where r_s is the probe radius, has to be fulfilled so that the cylindrical probe theory applies. Our measurements led to λ_{De} values between 0.15 and 0.20 mm. Since they are of the order of r_s (≈ 0.15 mm), we accept the plasma parameters calculated above.

An unavoidable problem concerning the use of an electrostatic probe to study methane plasma, and in general any hydrocarbon discharge, is its contamination through the deposition of an insulating thin film onto probe's surface during measurement. The disadvantageous effect of this coating consists of a continuous change of measuring conditions. Furthermore, such insulator introduces an extra resistance that increases significantly the effective decaying time constant, τ , of the probe [Deguchi M., 2002]:

$$\tau = R \cdot C = \rho \frac{d}{S} \cdot \varepsilon \frac{S}{d} = \rho \cdot \varepsilon \quad (5.5)$$

where the electric parameters concerning the properties of contaminating film are: resistance, R ; capacitance, C ; resistivity, ρ ; film thickness, d , and film area, S . Figure 5.3 shows a schematic of an insulated Langmuir probe.

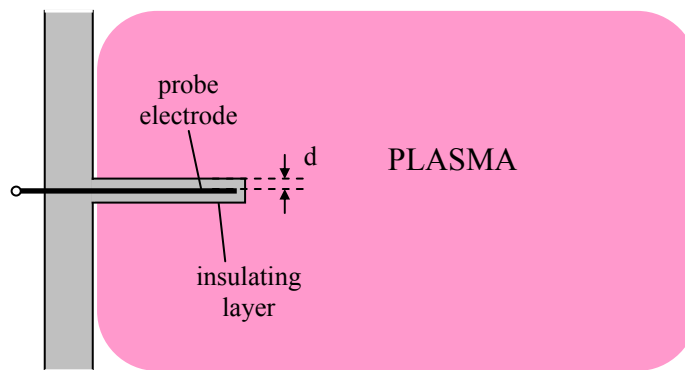


Figure 5.3: Schematic of electrostatic probe with contaminating film on it.

In some cases, this parameter becomes about 10^{-1} s or longer, which is five orders of magnitude greater than the resolution time of our measurements. Thus, it supposes a limit to the resolution time in diagnostics of pulsed plasmas because avoids synchronous operation between pulsed-DC supply and Langmuir probe. The solution adopted to overcome this contamination problem and, therefore, obtain stable measurements, consists of establishing a cleaning protocol. Prior to Langmuir probe measurements, the probe was retracted and the chamber was cleaned by oxygen plasma of 0.6 Pa for 5 minutes in order to remove carbon contamination on the walls. Next to this, the probe was introduced into the reactor and its tip was cleaned in an argon RF discharge etching process [Cali F.A., 1995] to remove carbon films of the tungsten probe. Although oxygen plasma is more effective at removing carbon contamination, it is not appropriate to clean W probes because of their possible oxidation.

During plasma cleaning, the W tip becomes the cathode and emits a strong light. The plasma surrounding the probe during cleaning process contains a high ion density and suffers an intense Ar^+ bombardment.

5.3. Study of a pulsed-DC methane glow discharge

The aim of this section is to analyse the main characteristics of the mid-frequency (100 kHz) pulsed plasma of methane as a function of the process parameters. It is also interesting to compare plasma parameters recorded by the Langmuir probe with those set in the RF process. Monitoring of the plasma is performed in the time-resolved mode. Therefore, its electric characterisation will be calculated by averaging the parameters measured in the plasma.

5.3.1. Electric parameters

The temporal evolution of the cathode voltage in a 100 kHz pulsed methane discharge sustained at 10 Pa is plotted in figure 5.4. As described in chapter 3, the pulsed voltage signal waveform consists of a muffled oscillating motion. Only the first oscillating semi-period of the signal is visible because its stabilization time is longer than the pulse frequency.

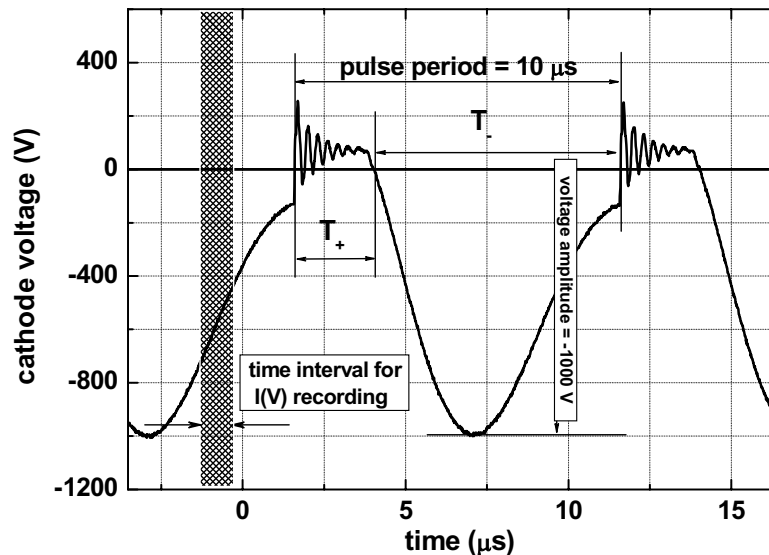


Figure 5.4: Voltage signal waveform driven to the cathode by the pulsed-DC source in a 10 Pa CH_4 discharge. Two regions are distinguished within the pulse: one positive (T_+) and another negative (T_-), the latter being the most energetic in all the cases. The pulse frequency is 100 kHz and $T_+ = 2016$ ns.

The voltage signal waveform supplied by the pulsed-DC source in methane discharge comprises two well-defined temporal regions within the pulse: a positive region and a negative one, let us say T_+ and T_- , respectively. The latter is the most energetic, as shown

by the large amplitude achieved at the peak voltage zone. T_+ was set to 2016 ns, and so duty cycle was around 80%. The resolution time of the measurements is 1 μ s. Each I(V) characteristic has been recorded in a time interval whose width appears shadowed in figure 5.4. Since we have worked at 100 kHz, ten I(V) plots in total were needed to sweep a complete cycle.

Figure 5.5 shows the variations of peak voltage and the average values of voltage and current intensity, as a function of the pulsed-DC power driven to the substrate holder. Pulse frequency ranged between 100 and 200 kHz, whereas T_+ was fixed at 2016 ns. Thus, the duty cycle varied from 80% to 60%. Such values are supplied by the pulsed power generator. It is evidenced that intensity and voltage values can be adjusted by varying the pulse frequency at a given power level.

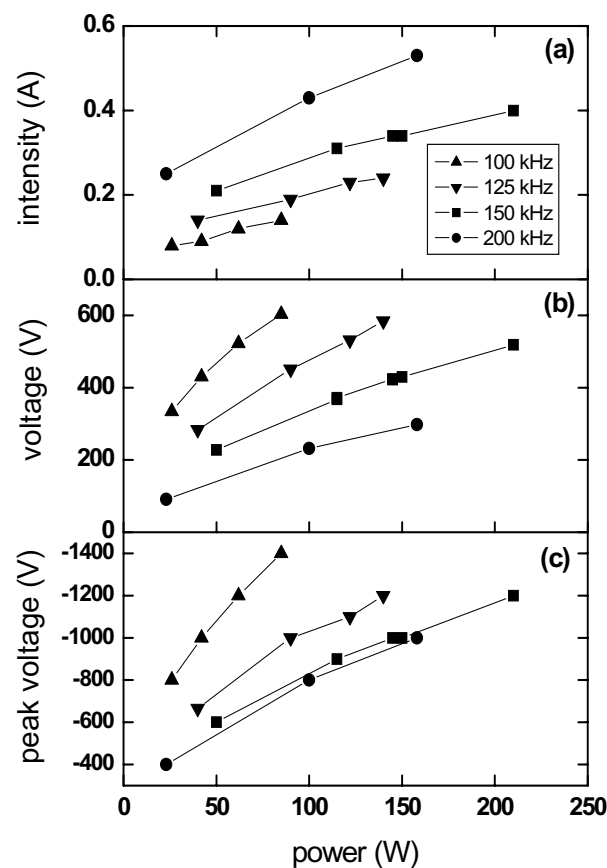


Figure 5.5: Power dependence of (a) the average current density supplied by the pulsed-DC generator, (b) the average voltage, and (c) the negative peak voltage amplitude or bias voltage, for different pulse frequencies.

We have estimated the effective load discharge impedance associated to this pulsed plasma. Its values for each frequency are obtained by calculating the voltage to intensity

ratios from the measurements in figure 5.5. As shows figure 5.6, this impedance decreases exponentially as frequency increases from 100 to 200 kHz. This behaviour is indicative of an enhanced plasma electron density as pulse frequency is increased. Therefore, we have demonstrated that pulse frequency is an important technological variable to tune the electric parameters of the discharge.

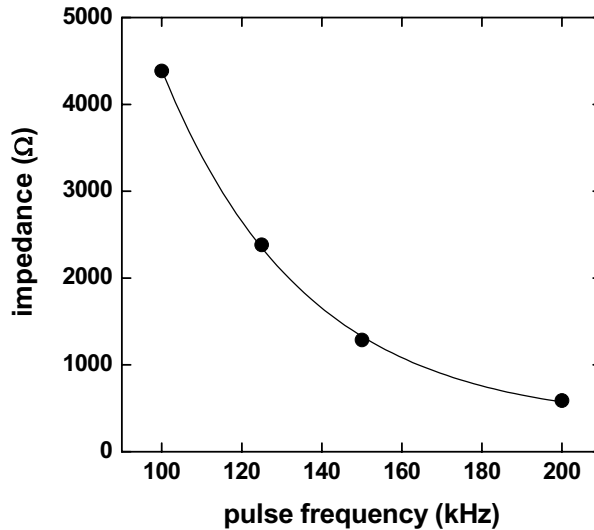
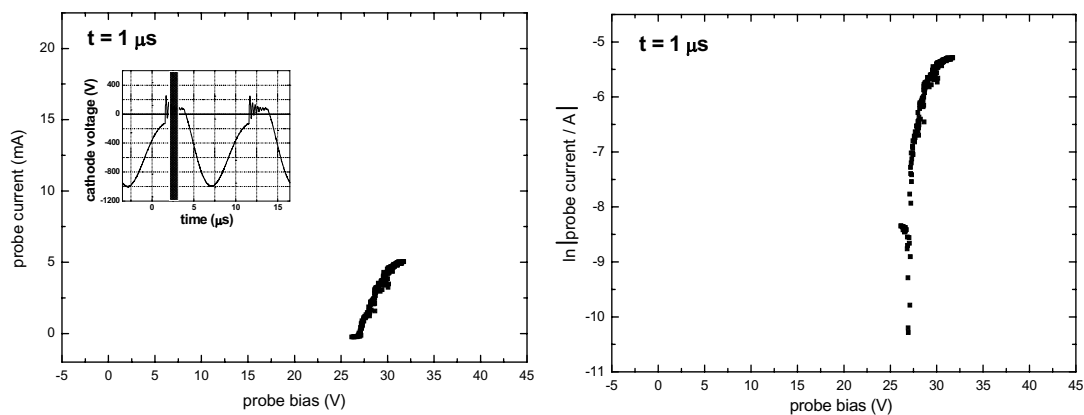


Figure 5.6: Variation of the effective discharge impedance with pulse frequency.

5.3.2. I(V) characteristics recorded in time-resolved mode

Time-resolved acquisitions of I(V) from a pulsed discharge biased at -900 V are shown in figures 5.7 and 5.8. Each curve is measured at each 1 μ s within the pulse period of 10 μ s. Figure 5.7 includes I(V) characteristics recorded during T_+ phase, which are accompanied by their logarithmic plots. The insets contain the pulse waveform, where the measured intervals appear shadowed.



(next page)

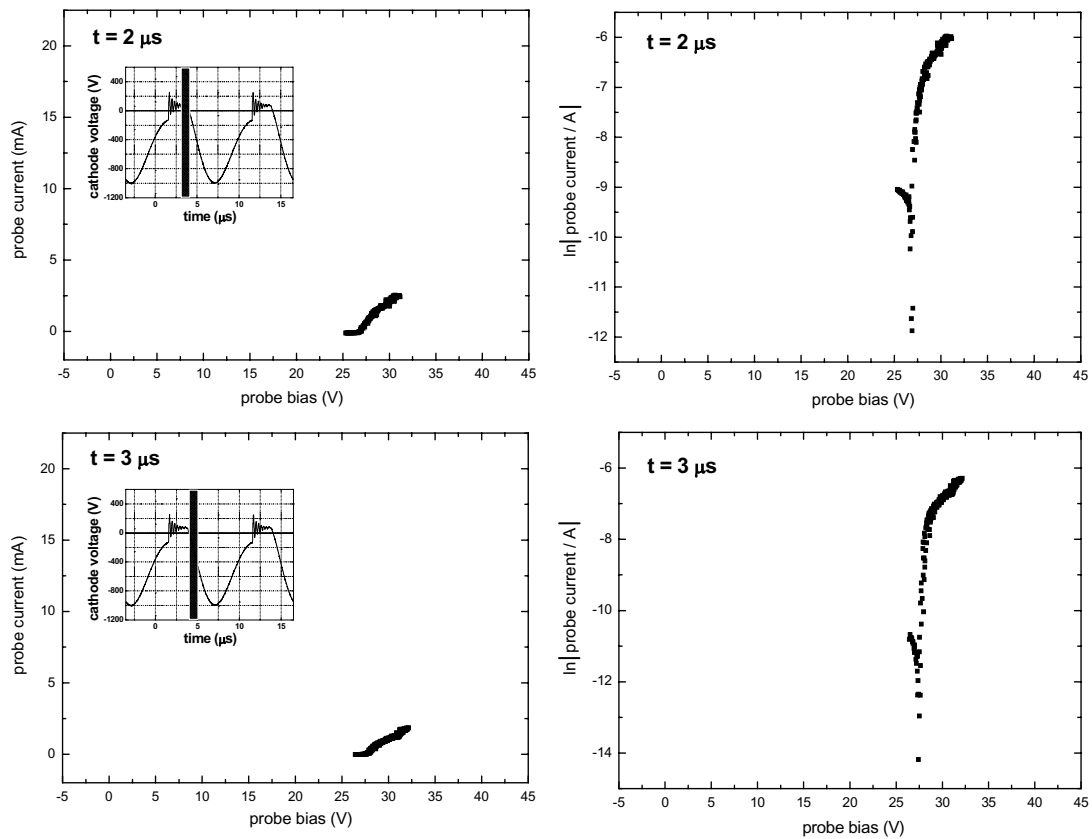
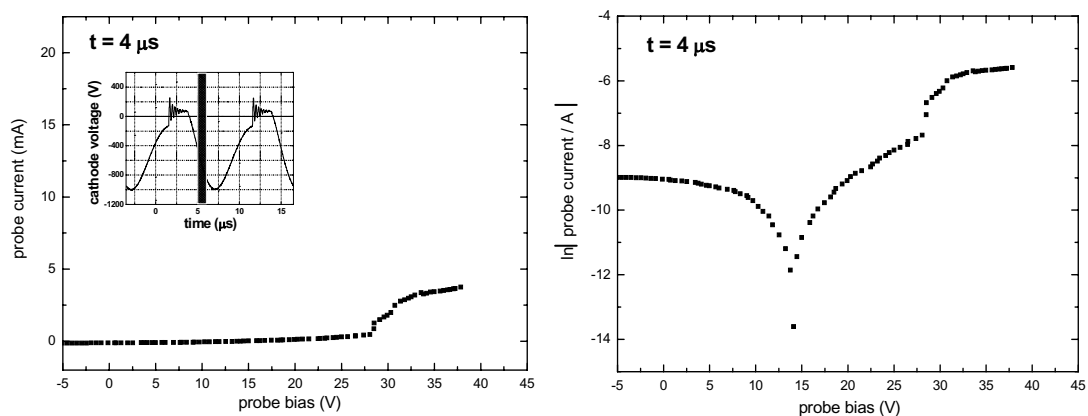
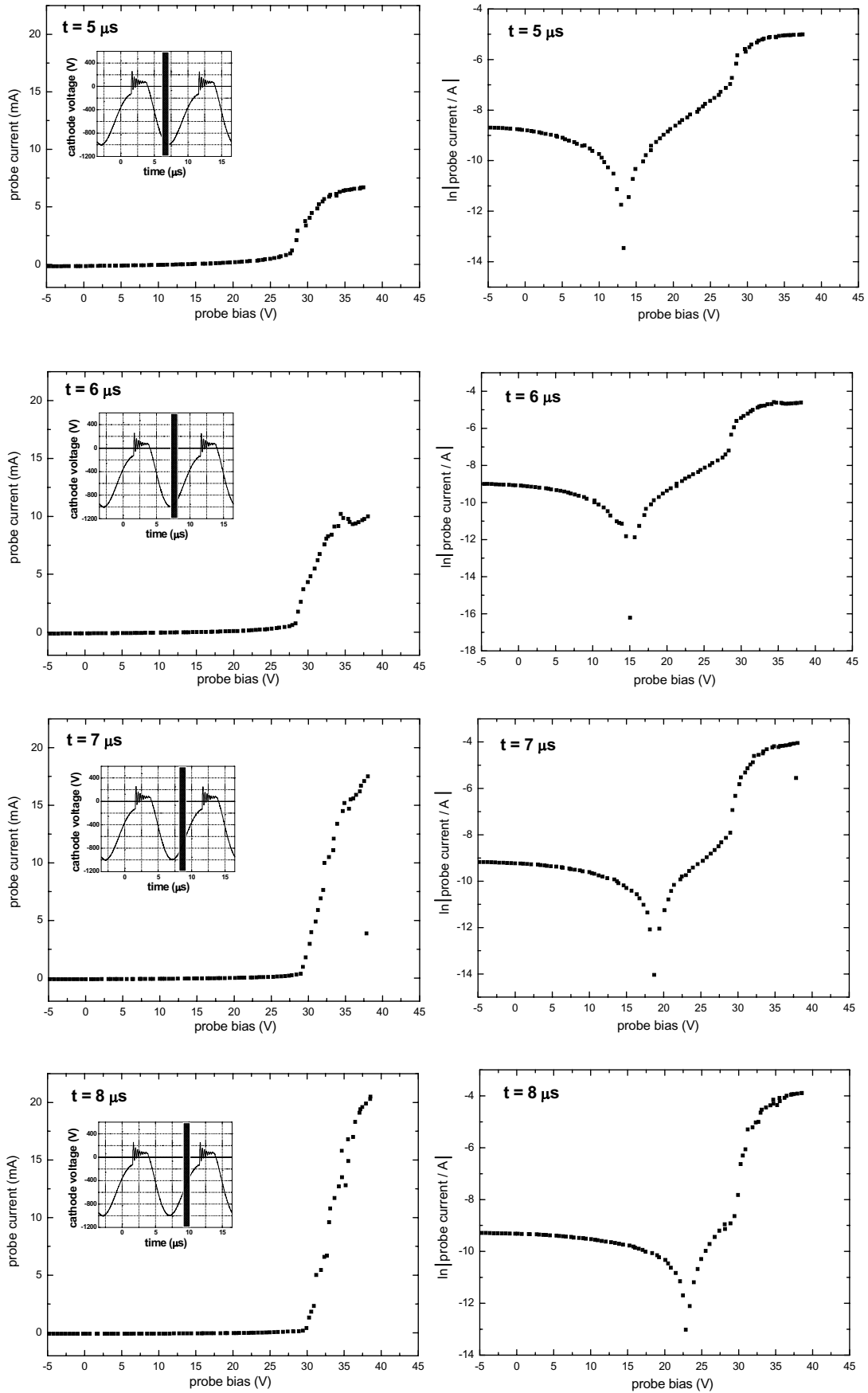


Figure 5.7: $I(V)$ curves corresponding to the low energy, T_+ phase from a pulsed-DC CH_4 plasma biased at -900 V.

Figure 5.8 shows $I(V)$ curves registered within the energetic stage of the pulse, T_- . Note the rather smooth evolution of these curves for the different pulse times. When compared to the curves in figure 5.7, $I(V)$ plots from T_- now present higher intensities at the electron conduction region. The signal to noise ratio has also increased. Thus, prospective data treatment for these T_- curves will be more accurate than for the T_+ ones. Plots from T_- phase also highlight a shape with a more complex structure, whose physical meaning will be discussed in the following section.



(next page)



(next page)

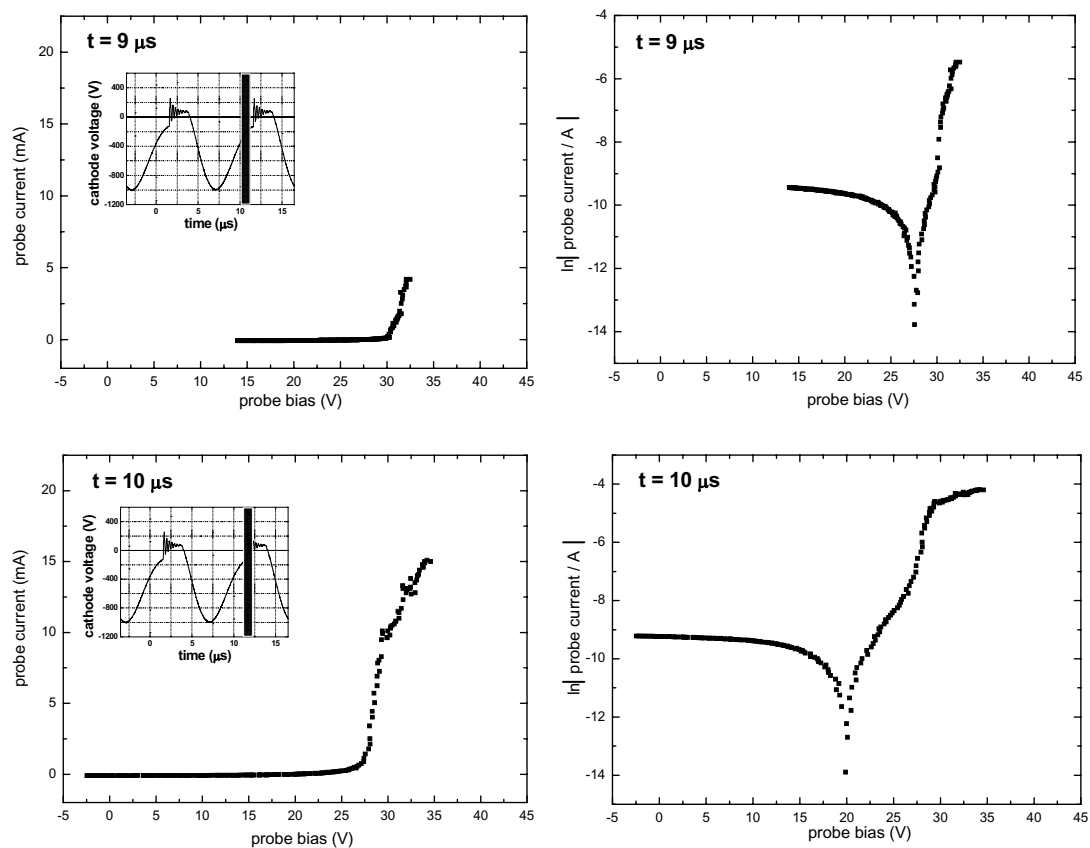


Figure 5.8: I(V) curves corresponding to the high energy, T_+ phase from a pulsed-DC CH₄ plasma biased at -900 V.

5.3.3. Fitting to a 2-temperature model

Figure 5.9(a) presents an I(V) characteristic measured within the T_+ phase. Concretely, it corresponds to the plasma state at -900 V peak voltage and $t = 3 \mu\text{s}$. As observed also for $t = 1, 2 \mu\text{s}$, the behaviour of the logarithmic plot in figure 5.9(b) is similar to the I(V) characteristic in the RF plasma studied in section 5.2. Hence, the model from equation 5.1 has also been adopted here to calculate the parameters of the plasma.

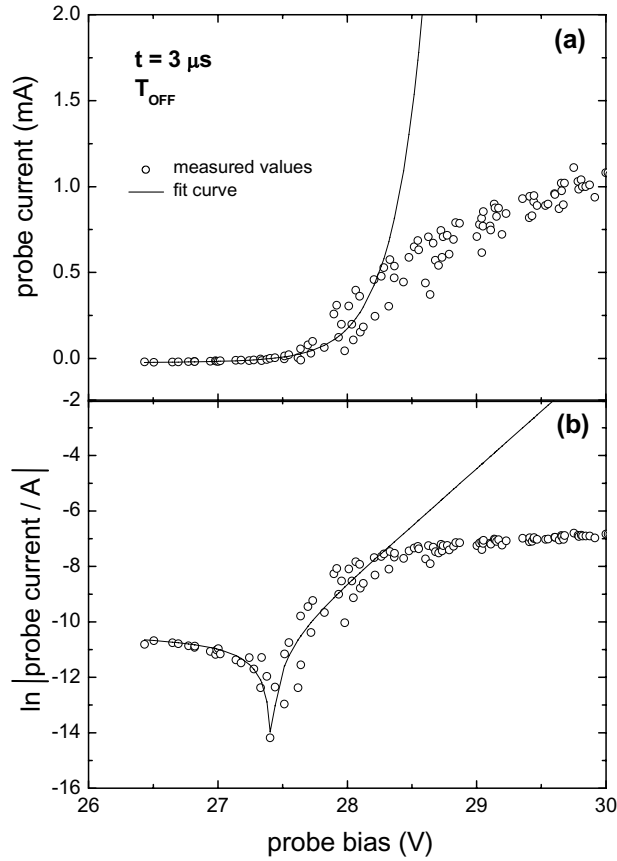


Figure 5.9: Measured probe characteristic in time-resolved mode from a 100 kHz CH₄ pulsed-DC discharge along with its fitted curve, plotted on (a) linear and (b) logarithmic scales. This I(V) corresponds to T_+ phase.

Figure 5.10(a) presents an I(V) profile measured at $t = 5 \mu\text{s}$, which is inscribed within the negative voltage region of the pulse, T_- . From an accurate analysis of this curve we can conclude that a fitting of an exponential function, like in the RF case or T_+ phase, is not satisfactory. Figure 5.10(b) presents the same I(V) plotted in logarithmic scale, and evidences the reason of this disagreement: the two slopes detected in the saturation region show the existence of more than one electron population. Every straight track in this region accounts for an electron group with a given temperature. Hence, the I(V) characteristics from pulsed discharges were adjusted to a two-temperature electron model [Corbella C., 2005d]:

$$i_e = C\sqrt{V_p - V} + i_e^{cold} \exp\left[\frac{e(V - V_p)}{kT_e^{cold}}\right] + i_e^{hot} \exp\left[\frac{e(V - V_p)}{kT_e^{hot}}\right] \quad (5.6)$$

whose parameters are analogues to those in the one-temperature model in section 5.2: i_e is the probe electron current; V is the probe bias; V_p is the plasma potential, identified as the maximum of the derivative of the I(V) curve; C is a constant that depends on ion density

(equation 5.3); e is the elementary charge; k is the Boltzmann constant; T_e^{cold} and T_e^{hot} are the temperatures of the cold and hot electron populations, respectively; i_e^{cold} and i_e^{hot} are the cold and hot electron current contributions to the plasma potential, and are respectively related to the electron densities of cold and hot groups, n_e^{cold} and n_e^{hot} :

$$i_e^{cold} = n_e^{cold} e A \left(\frac{k T_e^{cold}}{2 \pi m} \right)^{1/2} \quad (5.7)$$

$$i_e^{hot} = n_e^{hot} e A \left(\frac{k T_e^{hot}}{2 \pi m} \right)^{1/2} \quad (5.8)$$

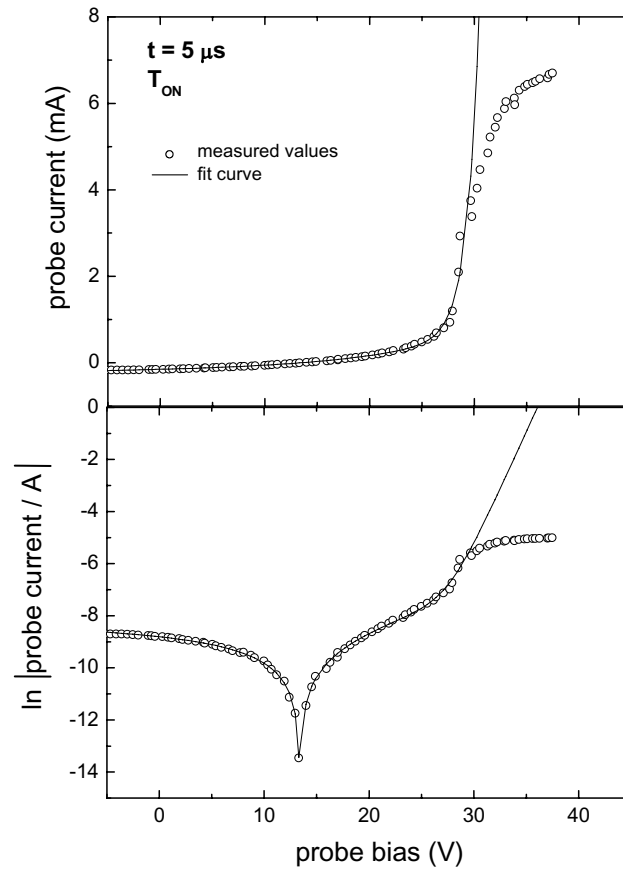


Figure 5.10: Measured probe characteristic in a time-resolved mode of a 100 kHz CH_4 pulsed-DC discharge plotted on (a) linear and (b) logarithmic scales. The solid line represents the fitted curve. This $I(V)$ corresponds to the T_e period.

Figure 5.11 is an example of $I(V)$, where two temperatures can be distinguished. Hence, the excitation of the plasma by low positive pulses and very energetic negative pulses induces the coexistence of two populations of cold and hot electrons.

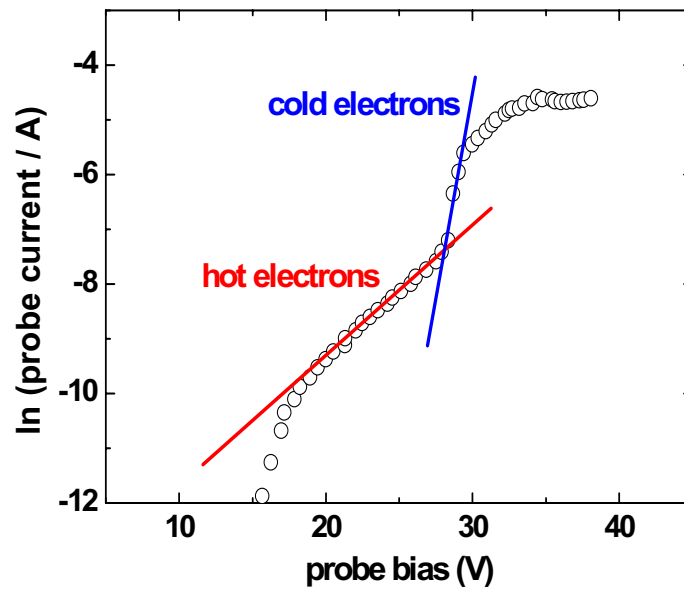


Figure 5.11: Example of $I(V)$ characteristic recorded with $1 \mu\text{s}$ of resolution time (at -900 V of peak voltage and $t = 6 \mu\text{s}$). The two slopes owe to the presence of hot and cold electron components.

5.3.4. Plasma parameters in the time-resolved mode

The plasma parameters were obtained from the fittings of the $I(V)$ curves to our model. Their time evolution within one pulse cycle using a peak voltage of -900 V is represented in figures 5.12, 5.14, 5.15 and 5.16, and their average values are displayed in figure 5.17. The voltage signal waveform is therein included with a dotted line. One should remember that the positive region is the shortest in time. There, a single electron population with a temperature of around 0.25 eV was measured. On the other hand, two electron populations were detected in the negative bias voltage region, as shown in figure 5.12.

The coexistence of two-temperature electrons was already observed in the case of DC magnetron sputtering plasma of He [Sheridan T.E., 1991]. This splitting takes place at the bias inversion zone of the pulse cycle, approximately $1 \mu\text{s}$ after the starting point of the negative region. The temperature of the hot group reaches nearly 10 eV and keeps stationary along the negative region, whereas the cold group keeps within the temperature of the positive region.

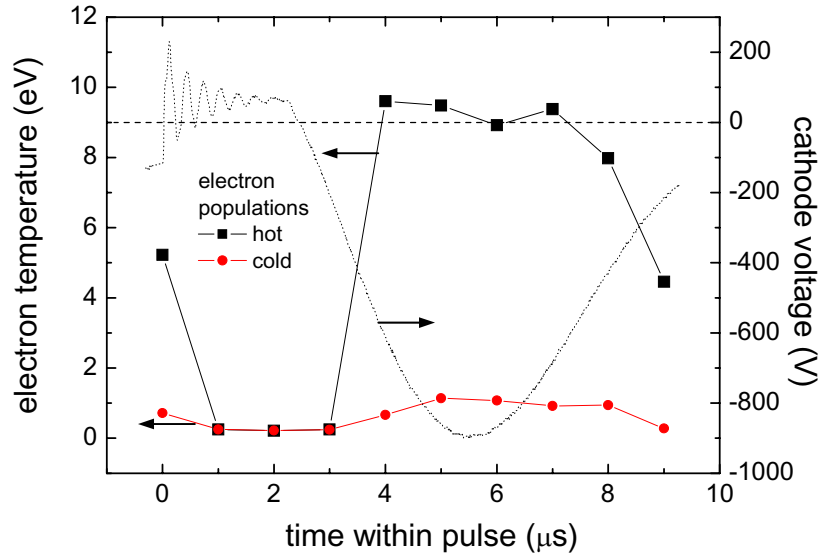


Figure 5.12: Monitoring of electron temperature within a pulse. Two electron populations are distinguishable in the negative pulse region.

The observed burst of hot electrons may arise from *stochastic heating*. This mechanism is promoted by the oscillation of the cathode sheath-edge, which supposes a channel for energetic electrons. Indeed, electrons are confined in the plasma bulk, within the space limited by plasma sheaths. Supposing elastic collisions, electrons that interact with the oscillating sheath-edges either lose or gain energy, as represented in figure 5.13.

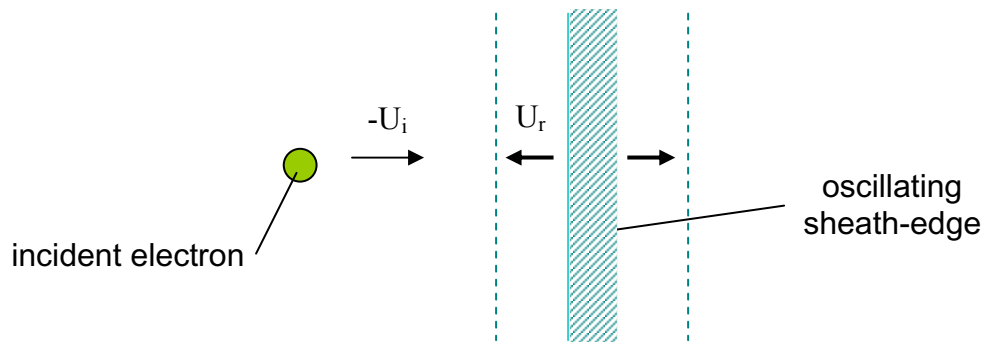


Figure 5.13: Electron colliding a plasma oscillating sheath (Fermi acceleration).

It has been shown that oscillating sheaths increase average electron energy through Fermi acceleration [Fermi E., 1949], which leads to a net electron heating [Glocker D.A., 1993]. Assuming elastic collisions between electrons and sheath-edges, the velocity of the outgoing electron, U_r , is:

$$U_r = -U_i + 2U_s \quad (5.9)$$

where U_i is the incident velocity and U_s is the velocity of the sheath-edge at the time of the collision. According to Fermi's arguments, on average the electrons will gain energy due

to the higher probability of head-on collisions as they bounce between the plasma sheaths [Gozadinos G., 2001].

Another study reported the formation of a single peak in electron temperature for an argon pulsed plasma in a magnetron system [Bradley J.W., 2001]. However, we have measured an almost constant hot electron temperature in the negative region. Such discrepancy is probably due to the absence of magnetron in our reactor, which facilitates the electron diffusion. In fact, a large number of hot electrons are able to reach the probe for a longer time because they are not trapped by any local magnetic field, so they contribute to probe current during all the energetic stage of the pulse.

Figure 5.14 shows that the electron density during the T_- of a pulse cycle is also divided into two groups, in agreement with the observation of two temperatures. The density related to cold electrons increases over one order of magnitude after the positive bias region, reaching $6.5 \cdot 10^{10} \text{ cm}^{-3}$, whereas the corresponding to the hot electrons is located between $2 \cdot 10^8$ and $1.0 \cdot 10^9 \text{ cm}^{-3}$. Electrons are confined in the plasma bulk during the discharge, and diffuse towards the reactor walls when plasma is switched off or weakened. This could be the reason for the electron depletion registered in the T_+ region. To obtain higher hot electron densities, and, thus, a more energetic plasma, it is suggested to add a magnetron into the cathode. In this way, the density of the hot group may even overcome that corresponding to the cold electrons in the magnetic trap region [Sheridan T.E., 1991].

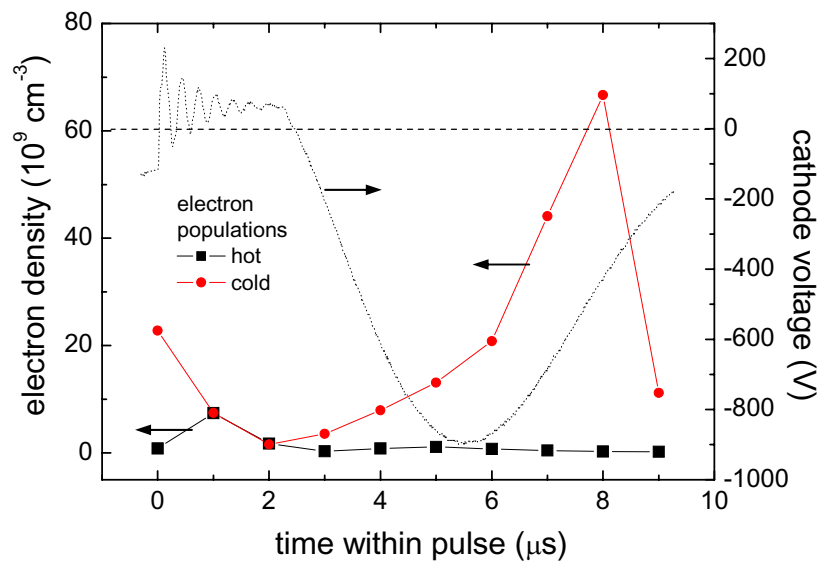


Figure 5.14: Evolution of electron density vs. time within a pulse.

In figure 5.15, the ion density shows a punctual growth in the positive region up to $1.34 \cdot 10^{11} \text{ cm}^{-3}$. This could be due to an effect of plasma weakening, associated to the interruption of electron confinement in the positive stage. Thus, the ions produced in positive pulses are confined in the plasma during T_+ , and deposited onto the cathode during the subsequent negative region of the pulse.

The delay of the ion density maximum with respect to the electronic peak could be a consequence of plasma instabilities owing to the pulsed signal. The existence of this unstable regime, together with the slow diffusivity of ions, which increases their response time to any perturbation, could account for this phase-shift. Although maximum values of ion and electron densities do not match during the same time interval, average values present the same order of magnitude, as shown in figure 5.18. Hence, the condition of plasma quasi-neutrality is preserved over each pulse cycle.

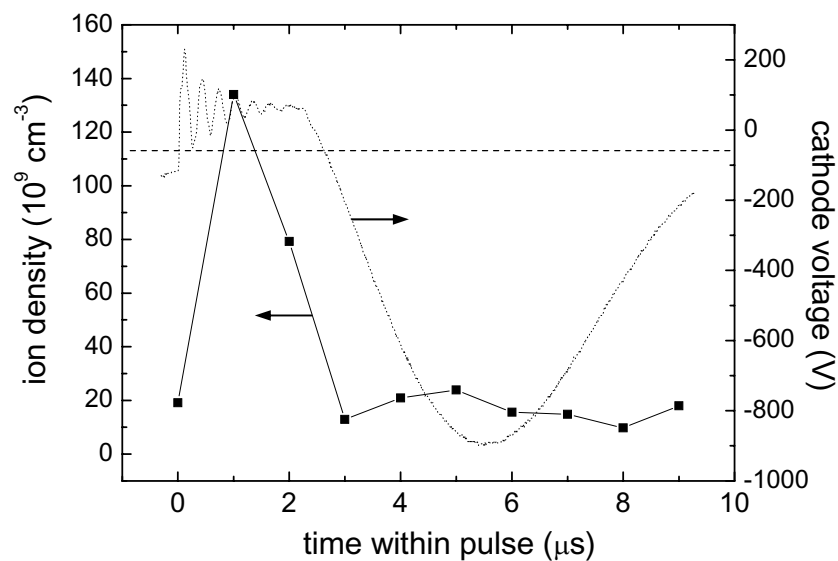


Figure 5.15: Behaviour of ion density within a pulse. It takes the highest values in the T_+ zone.

The CH_4 plasma potential reaches a value around 30 V in all bias values and varies very smoothly during a pulse cycle, as represented in figure 5.16. This behaviour, which indicates that the plasma is not extinguished in the reversal bias period, is beneficial for material processing because avoids cathode voltage spikes on the negative-going phase of the cycle and, therefore, prevents from electric arcing. A different behaviour is shown by

the floating potential, which follows a parallel evolution with the temperature of hot electrons.

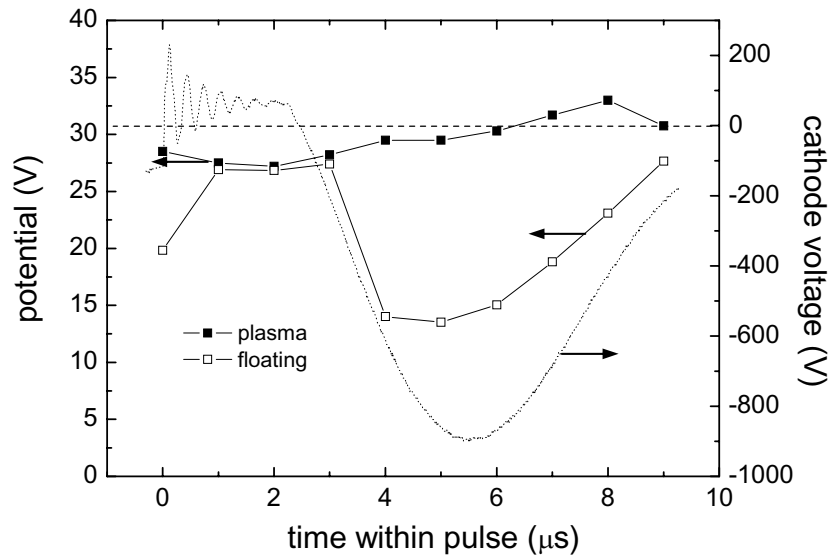


Figure 5.16: Plasma and floating potentials registered in time-resolved mode.

The evolution of the plasma parameters within a pulse cycle has also been studied for -700 and -1100 V peak voltage discharges. Both cases show behaviours similar to that of -900 V peak voltage. Nevertheless, average values present some differences. The effect of varying peak voltage on the average electron temperature is shown in figure 5.17. The two coexisting populations of cold and hot electrons show temperatures of approximately 0.5 and 5.5 eV, respectively, being the temperature a result from the high values (~ 10 eV) acquired during T_r region. The hot electrons experience a moderate increase up to 5.9 eV with the bias values, whereas the cold electrons do not show a definite trend.

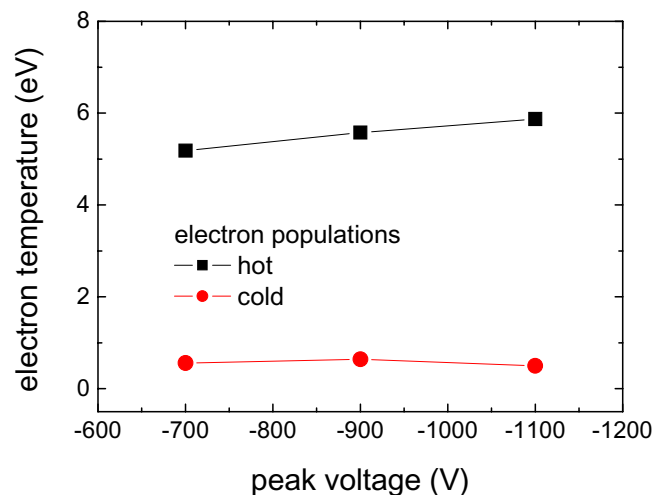


Figure 5.17: Evolution of temperatures of hot and cold electrons as a function of voltage peak amplitude of the pulsed-DC methane plasma.

We can observe the variation of average values for electron and ion densities in figure 5.18. The density of hot electrons is around $1.5 \cdot 10^9 \text{ cm}^{-3}$, whereas that of the cold ones shows an increase from $1.80 \cdot 10^{10}$ to $2.88 \cdot 10^{10} \text{ cm}^{-3}$. The ion density shows a uniform increase as well, and its values overcome always the density of cold electrons. According to these results, pulsed-DC discharges provide generally positively charged plasmas. We must take into account that such results have been obtained by assuming an ion mass of 17 a.m.u., which corresponds to the ion CH_5^+ , for the calculation of ion density.

Since the processes and reactions in a plasma take place far from equilibrium in a pulsed regime, the most abundant ion is expected to vary widely in time. Thus, further studies of plasma chemistry are needed to provide the time-varying distribution of species present in plasmas when powered by pulsed-DC energy. The knowledge of such distribution would permit us to obtain the ion density with high accuracy compared to the present situation that considers a constant ion mass.

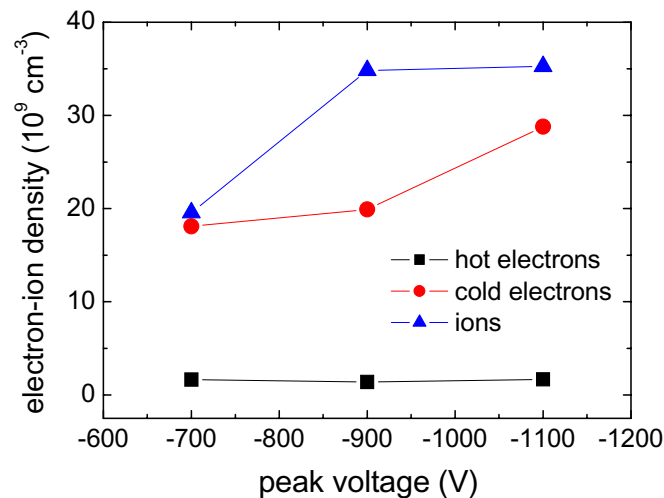


Figure 5.18: Variation of electron and ion densities with peak voltage of the pulsed-DC methane plasma.

Figure 5.19 shows that the plasma potential is located in the region of 30 V and increases smoothly with peak voltage, which is indicative of a more active plasma. On the other hand, the floating potential takes values around 20 V and tends to decrease.

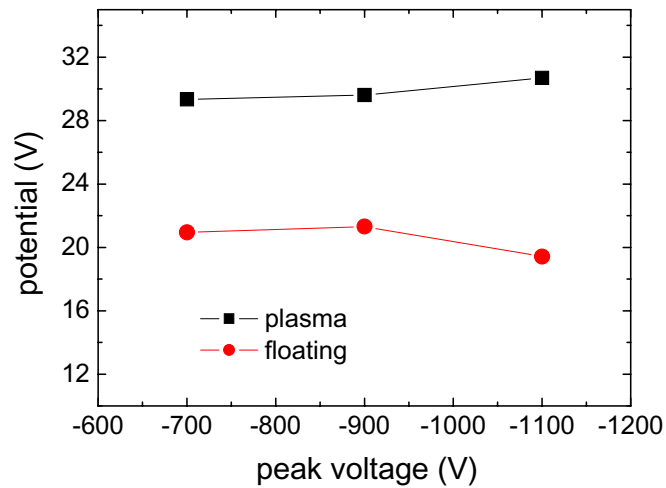


Figure 5.19: Evolution of plasma and floating potentials of the pulsed-DC methane discharge, as a function of peak voltage.

It is worth noting that RF-plasmas of CH_4 with -400 V of self-bias showed electronic temperatures below 2 eV and electron densities below $5 \cdot 10^9 \text{ cm}^{-3}$, which are up to 5 times lower than the typical cold electron densities of pulsed discharges. In addition, the ionic density of pulsed discharges reached values in the range $3.5 \cdot 10^{10} \text{ cm}^{-3}$, which again are higher than the ionic density for RF discharges (up to $1.9 \cdot 10^{10} \text{ cm}^{-3}$). These values are indicative of the greater density and intensity of the conditions of charged species bombardment in pulsed-DC glow discharges, when compared to the RF plasmas that are usually employed for the production of DLC films.

Summary and conclusions

- 1) A pulsed-DC methane glow discharge has been studied with Langmuir probe measurements in time-resolved mode. The coupling of a time-delay circuit facilitated an accurate monitoring of plasma parameters within a pulse of 100 kHz of frequency and a positive pulse time of 2 μ s.
- 2) The asymmetrical bipolar pulsed-DC voltage waveform consisted of a fixed positive pulse amplitude of 40 V followed by a variable negative pulse, whose peak amplitude was varied from -700 down to -1100 V.
- 3) The higher energies and stronger ionisation rates achieved by pulsed-DC methane discharges lead to an enhancement in the values of plasma parameters as compared with RF methane discharges.
- 4) Two electron populations are distinguished in the negative region of the pulse. The hot group achieves 10 eV and has a stationary density, whereas the cold population (\sim 1 eV) presents an electron density that is one order of magnitude higher at the negative region of the pulse.
- 5) The ion density shows a punctual growth in the positive region of the pulse. Although maximum values of ion and electron densities do not match the same time interval, average values present the same order of magnitude, and then the electric quasi-neutrality is preserved.
- 6) The methane plasma potential (\sim 30 V) varies smoothly during the cycle, indicating that the discharge was not extinguished in the reversal bias period, whereas the floating potential evolves in parallel with the hot-electron temperature.

